Article

Alzheimer's Protective A2T Mutation Changes the Conformational Landscape of the Aβ_{1-42} Monomer Differently Than Does the A2V Mutation

Payel Das,[1,*] Brian Murray,[2] and Georges Belfort[2]
[1]Soft Matter Theory and Simulations Group, Computational Biology Center, IBM Thomas J. Watson Research Center, Yorktown Heights, New York; and [2]Howard P. Isermann Department of Chemical and Biological Engineering and Center for Biotechnology and Interdisciplinary Studies, Rensselaer Polytechnic Institute, Troy, New York

ABSTRACT The aggregation of amyloid-β (Aβ) peptides plays a crucial role in the etiology of Alzheimer's disease (AD). Recently, it has been reported that an A2T mutation in Aβ can protect against AD. Interestingly, a nonpolar A2V mutation also has been found to offer protection against AD in the heterozygous state, although it causes early-onset AD in homozygous carriers. Since the conformational landscape of the Aβ monomer is known to directly contribute to the early-stage aggregation mechanism, it is important to characterize the effects of the A2T and A2V mutations on Aβ_{1-42} monomer structure. Here, we have performed extensive atomistic replica-exchange molecular dynamics simulations of the solvated wild-type (WT), A2V, and A2T Aβ_{1-42} monomers. Our simulations reveal that although all three variants remain as collapsed coils in solution, there exist significant structural differences among them at shorter timescales. A2V exhibits an enhanced double-hairpin population in comparison to the WT, similar to those reported in toxic WT Aβ_{1-42} oligomers. Such double-hairpin formation is caused by hydrophobic clustering between the N-terminus and the central and C-terminal hydrophobic patches. In contrast, the A2T mutation causes the N-terminus to engage in unusual electrostatic interactions with distant residues, such as K16 and E22, resulting in a unique population comprising only the C-terminal hairpin. These findings imply that a single A2X (where X = V or T) mutation in the primarily disordered N-terminus of the Aβ_{1-42} monomer can dramatically alter the β-hairpin population and switch the equilibrium toward alternative structures. The atomistically detailed, comparative view of the structural landscapes of A2V and A2T variant monomers obtained in this study can enhance our understanding of the mechanistic differences in their early-stage aggregation.

INTRODUCTION

Alzheimer's disease (AD) is the most common form of dementia, affecting nearly 38 million people worldwide, a figure that is predicted to double over the next 20 years. The pathological hallmarks of AD are the aberrant deposition of extracellular senile plaques comprised of amyloid-β (Aβ) peptides and intracellular neurofibrillary tangles (1). Proteolytic cleavage of the amyloid precursor protein generates Aβ peptides of different lengths (39–43 residues), among which Aβ_{1-40} and Aβ_{1-42} are the major isoforms, with Aβ_{1-42} being more aggregation-prone and toxic than Aβ_{1-40} (2). The molecular process underlying AD, as outlined in the amyloid β hypothesis, involves an imbalance between production and clearance of Aβ. This imbalance results in accumulation of amyloid plaques comprised of Aβ aggregates. The abnormal aggregation of Aβ peptides into β-sheet-rich fibrils involves a heterogeneous ensemble of oligomeric intermediates, all of which are found to be neurotoxic (3). Aβ toxicity originates from a number of factors, including formation of ion channels (4), oxidative stress (5), and interaction with receptors (6). NMR studies (7–10) suggest that Aβ_{1-42} fibrils model as parallel-stacked hairpin-like structures. The hydrophilic N-terminus (residues 1–16) appears unstructured in those fibril structures, whereas the two hydrophobic patches (residues 17–20 and 30–40) form U-shaped conformations comprised of two intermolecular, parallel, in-register β-sheets separated by a hydrophilic turn region (residues 22–29).

Most proposed pathways for the initial stages of Aβ amyloid fibril formation suggest some conformational change (misfolding) of the intrinsically disordered Aβ monomer, resulting in an activated monomer that then recruits other Aβ molecules to form low-n oligomers (11). Based on the protease-resistant nature of residues A21–A30, this region was proposed as the nucleus site for Aβ monomer misfolding (activation) (12). A link between monomer misfolding and aggregation propensity and toxicity has been proposed based on experiments (13–16) and simulations (17–26) of the naturally occurring alloforms. Those alloforms contain substitutions that occur mainly within the turn region (residues 22–30). Because of the disordered structure of the N-terminus in the fibril structure, the role of this region in aggregation, toxicity, and pathogenesis was considered for a long time to be negligible (27) and therefore remained largely unexplored. However, several recent reports indicate the possible importance of the N-terminus in Aβ structure, association, and toxicity (28–30). A novel structural motif

Submitted October 2, 2014, and accepted for publication December 4, 2014.
*Correspondence: daspa@us.ibm.com
Editor: David Eliezer.
© 2015 by the Biophysical Society
0006-3495/15/02/0738/10 $2.00
http://dx.doi.org/10.1016/j.bpj.2014.12.013

of triple β-sheet within $A\beta_{1-42}$ amyloid oligomers has been reported with minimal exposure of hydrophobic residues, in which association was found between the N-terminus and residues 17–22 (31). Antibodies that specifically bind to the N-terminus are known to effectively interact with both soluble and insoluble forms of $A\beta$ (32). Amyloid inhibitor tetrapeptides are also known to bind at the $A\beta$ N-terminus (33). Two N-terminal mutations, English (H6R) and Tottori (D7N), are reported to alter the monomer misfolding and produce oligomers that are toxic compared with the wild-type (WT) (16). A few recent studies have also suggested the importance of the extreme N-terminus. Experiments reported delayed assembly kinetics and compactness of the D1Y-substituted $A\beta_{40/42}$ peptides (34) and higher toxicity of an A2F variant (35), a consequence of a more hydrophobic N-terminus. It is known that the double mutation D1E/A2V affects $A\beta_{1-40}$ fibrillation (36). Pyroglutamate-modified $A\beta$ ($A\beta$(pE3-42)) peptides have also emerged as potential key factors in AD pathology due to their abundance in the AD brain, high aggregation propensity, stability, and cellular toxicity (37). A familial A2V mutation has been reported to cause dementia in homozygous carriers, whereas heterozygous carriers were found to be protected (38). The co-incubation of WT and A2V $A\beta_{1-42}$ peptides was shown to inhibit toxicity in the same study (38). The A2V $A\beta_{1-42}$ also has been shown to have a very different aggregation pathway involving annular oligomers with higher hydrophobic exposure and stronger toxicity compared to the WT; the A2V peptides more rapidly formed a structured oligomer, as demonstrated by dynamic light-scattering experiments (39).

Recently, a rare A2T variant was found to protect against AD and cognitive decline in the elderly without AD (40). This is thought to represent the first example of an $A\beta$ variant that confers protection against AD. The prevailing hypothesis for its protective action is that the mutation (A673T in the amyloid precursor protein or A2T in $A\beta$), close to the β-secretase cleavage site, lowers $A\beta$ production, thereby balancing production with clearance. However, the reported lowering in production was a moderate 20% in heterozygous carriers (40). The downstream effects of this mutation could also be vital to its protective behavior (41).

The effects of the A2V and A2T mutations on $A\beta$ aggregation and toxicity have just started to emerge, and reports appear somewhat controversial. Two recent studies that employed thioflavin T (ThT) fluorescence monitoring suggest very different effects of the A2T mutation on $A\beta_{1-42}$ aggregation (42,43). Benilova et al. showed no change in $A\beta_{1-42}$ aggregation upon either A2T or A2V mutation (43). On the other hand, the results from Maloney et al. suggested a lower aggregation propensity of A2T $A\beta_{1-42}$ when compared to both WT and A2V with similar aggregation profiles (42). In the context of $A\beta_{1-40}$, A2T has been shown to aggregate faster (43,44) or similarly (42) compared to WT. On the other hand, A2V $A\beta_{1-40}$ exhibited faster aggregation than the WT (38,42,43). The effects of those mutations on aggregation also have been analyzed in combination with the WT peptide. Although 1:1 mixture of WT/A2V $A\beta_{1-42}$ showed intermediate aggregation compared to the pure solutions in a study by Messa et al. (39), the same mixture was reported by Benilova and colleagues (43) to demonstrate fast aggregation similar to that observed for WT $A\beta_{1-42}$. The latter group reported that a 1:1 WT/A2T mixture exhibited no change in aggregation kinetics (43), but Maloney et al. found an intermediate effect (42).

Maloney et al. (42) also compared the toxicity of WT, A2V, and A2T peptides to cultured neurons and found that WT and A2T peptides exhibited similar toxicity, whereas A2V had somewhat lower toxicity. This is to some extent counterintuitive and contradictory to what was reported for the A2V $A\beta_{1-42}$ by Di Fede et al. (38). Taken together, the effects of A2V and A2T mutations on early aggregation and toxicity are still not fully clear and seem to be very different depending on the isoform ($A\beta_{1-40}$ versus $A\beta_{1-42}$) and experimental conditions. It is also possible that the current experiments are not sensitive enough to capture the effects of those mutations in the more hydrophobic, aggregation-prone, and toxic $A\beta_{1-42}$ isoform.

Given the protective and causative effects associated with the A2V and A2T substitutions and the established link between monomer misfolding and early aggregation, it is crucial to obtain a comparative view of the conformational landscapes of those two variants and the WT $A\beta_{1-42}$ full-length monomers. Even with the sophistication of modern techniques, experimental characterization of the monomeric $A\beta$ peptides remains challenging due to the intrinsically disordered and rapidly interchanging nature of the system. On the other hand, molecular dynamics (MD) simulations at different resolutions have been widely used to complement experiments (45) in providing detailed information on the structure of various $A\beta$ species ranging from monomers (23,46–50) to oligomers (51,52) to protofibrils (53) to fibrils (54). Interactions of different $A\beta$ species with toxicity and aggregation inhibitors (55–57) and with lipid bilayers (58,59) also have been studied using MD. In this study, we have performed extensive all-atom replica-exchange molecular dynamics (REMD) simulations of WT, A2V, and A2T $A\beta_{1-42}$ in explicit water to characterize the monomeric ensemble. To our knowledge, this is the first study comparing the structural landscapes of the A2T and A2V $A\beta_{1-42}$ monomers. Our simulations reveal an enhanced double-hairpin population in A2V due to hydrophobic clustering between the N-terminus and distant hydrophobic patches. In contrast, the A2T mutation engages the N-terminus in an unusual set of long-range electrostatic interactions with residues such as K16 and E22, resulting in a population of unique conformations that comprise only the C-terminal hairpin. These findings imply that the A2X (X = V or T)

mutations situated within the mainly disordered N-terminus can dramatically alter the WT monomeric conformational landscape by globally rewiring the intramolecular interaction network within Aβ_{1-42}.

MATERIALS AND METHODS

Details of the MD simulations regarding system setup, simulation parameters, simulation length, and so forth can be found in the Supporting Material. The total number of replicas used was 64, and each replica was 175 ns long, resulting in an aggregate simulation time of 11.2 μs per system. A number of convergence checks were performed (see the Supporting Material).

RESULTS

In this work, we compare in silico the monomeric conformational ensemble of the A2V and A2T Aβ_{1-42} variants with that of WT by performing extensive atomistic REMD simulations in explicit water. All three variants exhibit similar secondary structure propensity, with coils and turns being prevalent (see Fig. S3 *a* in the Supporting Material). The secondary-structure propensity values for WT are ~30% coil, ~45% turn, and ~18% β-strand; A2V and A2T show similar values. This estimated composition for the WT system in this study agrees well with an earlier report (20), implying that the sampling obtained using the protocol described here represents the WT monomeric structure reasonably and consistently well. The ensemble-averaged secondary structure per residue for each variant is shown in Fig. 1, *a–c*. The residue-based secondary-structure propensity analysis (Fig. 1, *a–c*) suggests a primarily disordered N-terminal region (residues 1–15) for all three variants, with a strong turn character around residues 8–9 and 13–15 and a small (5–10%) β-strand propensity in the first 12 residues. Some helical structure near residues 12–16 is also observed. Residues 17–20 (the central hydrophobic cluster (CHC)) and 31–40 show high β-strand propensity ($\geq$25%) in addition to a predominant turn around residues 23–30 in the WT (Fig. 1 *a*), consistent with the reported strand-loop-strand (SLS) structure of Aβ_{10-35} (60). Interestingly, A2V demonstrates higher β-strand propensity within residues 16–20, 30–35, and 39–41 compared with the WT. A significant increase in the turn propensity compared to the WT also can be noticed in residues 23–30 and 36–37 of A2V (Fig. 1 *b*). On the other hand, the β-strand propensity is found to be lower in A2T around residues 18–19, 31–32, and 36–39 (Fig. 1 *c*). In addition, the turns around residues 23–30 and 36–37 appear more prominent in A2T. These data indicate that a mutation in the extreme N-terminus (at position 2) can alter the secondary structural preference of the distant hydrophobic regions (the CHC and the C-terminus).

The C_α-contact map (Fig. 1 *d*, *upper triangle*) reveals the presence of strong antidiagonal contacts between the CHC and C-terminus, suggesting a β-hairpin formation in the

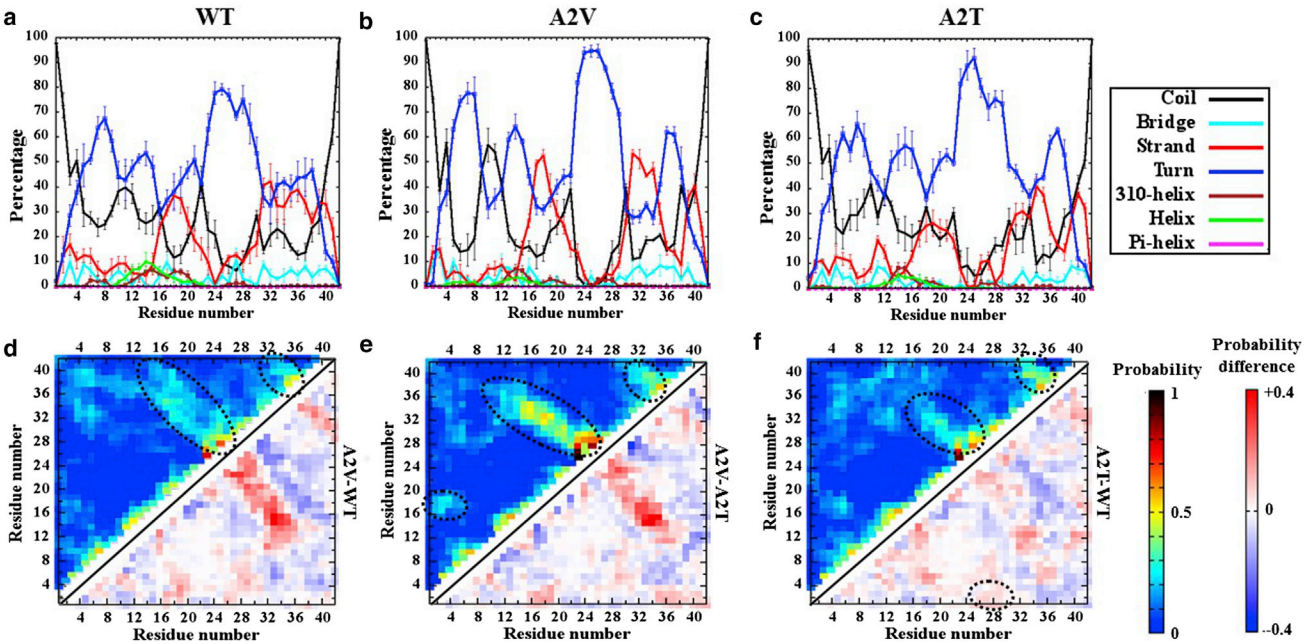

FIGURE 1 Secondary and tertiary structure. (*Top*) Secondary structure per residue averaged over the production ensemble: (*a*) WT, (*b*) A2V, and (*c*) A2T. Colors used are shown on the right. The standard deviations were estimated by splitting the data in four equal sets. (*Bottom*) Tertiary contact maps: (*d*) WT, (*e*) A2V, and (*f*) A2T. (*Upper triangle*) Ensemble-averaged probability of interresidue Cα-Cα contact formations (nonsequential contacts, i.e. $|i-j| \geq 3$, are only shown) are colored according to the color map shown on the right. (*Lower triangle*) Arithmetic difference between the contact probabilities for each pair of Aβ variants colored according to the color map shown on the right. Black dotted circles highlight the two sets of antidiagonal contacts as well as the crucial contacts involving residues 1–5, which help discriminating the variants. To see this figure in color, go online.

WT, consistent with earlier simulations (60). β-hairpin formation of residues 17–36 during early Aβ aggregation has been further supported by an affibody-Aβ complex structure (61) and by the presence of a turn-like structure at residues 25–29 in Aβ oligomers (62). Additional antidiagonal contacts appear prevalent in the C-terminal region between residues 33–36 and 39–41, indicative of a second β-hairpin motif. These results imply a double-hairpin topology, in agreement with the simulations performed by Rosenman et al. (20). Long-range interactions between two termini (residues 1–8 and 32–42) are observed in addition to some contacts between the CHC and the extreme N-terminus (residues 1–5). Highly probable local contacts consistently appear in the turn regions.

Fig. 1 *e* (*upper triangle*) reveals a more robust nature of those β-hairpin interactions in A2V compared to the WT, suggesting a favored population of double-hairpin structures in A2V. The long-range interactions between the N-terminus (residues 1–4) and the CHC are stronger in A2V (Fig. 2 *b*, *upper triangle*) compared with the WT. The difference contact map (Fig. 1 *d*, *lower triangle*) further reveals a register shift toward the N-terminus in A2V compared with the WT for both sets of antidiagonal interactions.

In the A2T variant (Fig. 1 *f*, *upper triangle*), the antiparallel β-hairpin interactions between the CHC and residues 30–35 are weaker than in the WT, whereas the C-terminal β-hairpin appears more robust. Also, a cluster of contacts between residues 5–7 and the CHC is observed in A2T. Interactions between residues 1–4 and 34–42 appear weaker in A2T than in the WT (Fig. 1 *f*, *lower triangle*). However, residues 1–4 of A2T make contact more frequently with the 23–30 turn (Fig. 1 *f*, *lower triangle*, *dashed circle*); in general, those contacts are weak. At least 25% of those contacts occur with a $\geq$10% probability for the A2T variant, compared to 7% probability in the WT and A2V. Taken together, these results suggest that the A2V/T substitution primarily alters 1) the β-hairpin interactions between the CHC and the C-terminus, termed $NC_{CHC\text{-}CTR}$ and 2) the interactions between the N-terminus (Ntr) (residues 1–5) and the CHC, termed $NC_{Ntr\text{-}CHC}$.

In the following, we compare the potential mean force (PMF) plots (Fig. 2) to discriminate between the conformational ensembles of different variants. It should be noted that as all three peptides are intrinsically disordered, it is nontrivial to choose an optimal set of reaction coordinates for defining their free-energy landscapes. Since from the above analysis, the two sets of contacts, namely $NC_{Ntr\text{-}CHC}$

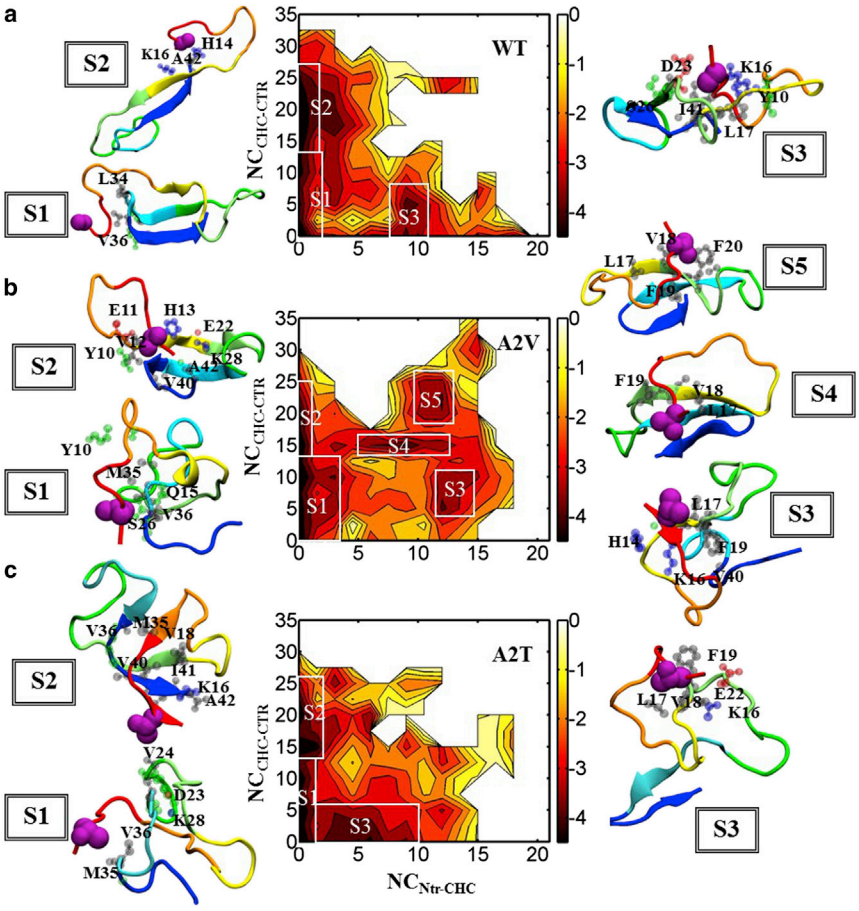

FIGURE 2 Potential of mean force (PMF) plots: (*a*) WT, (*b*) A2V, and (*c*) A2T. Two-dimensional PMF plots as a function of number of contacts between the Ntr (residues 1–5) and the CHC (residues 16–21), $NC_{Ntr\text{-}CHC}$, and number of contacts between the CHC and the C-terminal region (residues 31–42), $NC_{CHC\text{-}CTR}$. Each contour level represents 0.5 kcal/mol. White squares denote the discrete regions on the PMF plots individually representing $\geq$5% of the production ensemble. The representative conformation of the largest cluster for each of those regions is shown using cartoon representation colored with a red-to-blue rainbow spectrum from the N- to C-terminus. Residue 2 is shown in purple spheres, whereas the residues forming long-range contacts with the N-tr are shown using CPK representation. A 5 Å cutoff between heavy atoms is used for this purpose. The residues are colored according to their types (hydrophobic, *gray*; polar, *green*; basic, *blue*; acidic, *red*). To see this figure in color, go online.

and $NC_{CHC\text{-}CTR}$, appear to capture notable differences in the tertiary contact probabilities among variants, we estimated the PMFs as a function of them (see the Supporting Material). The WT PMF plot reveals distinct features of the most populated regions (regions S1–S3) (Fig. 2 *a*, *white boxes*) of the landscape. The S1 region corresponds to the structures with strongly limited $NC_{Ntr\text{-}CHC}$ and $NC_{CHC\text{-}CTR}$ contacts. Structures with robust CHC-CTR interaction accompanied by a few ($\leq$5) Ntr-CHC contacts populate the S2 region. In contrast, S3 conformations exhibit stronger Ntr-CHC interaction but lack substantial CHC-CTR contacts, and they are much less populated (compared to S1 and S2). We also performed a cluster analysis with a 3 Å Cα-RMSD cutoff distance on those discrete regions. The definition criteria, population size, and cluster analysis results for those regions are listed in Table S1, demonstrating that those structures all together represent >75% of the total ensemble for each system. The total number of clusters and the size of the top five clusters show that the S1 structures are more disordered than S2 structures, whereas S3 can be well represented by a single cluster. The representative structure for the largest cluster of each region is shown in Fig. 2 *a*. Additional representative structures, as well as the tertiary contact maps and the residue-based secondary-structure propensities, can be found in Fig. S4. Those data confirm that the WT S1 conformations are mostly disordered and show very little secondary and tertiary structure (Fig. S4 *a*). The only structured region in the S1 conformations is the C-terminus, with a 20% β-hairpin population. In contrast, both sets of hairpin contacts are evident in S2 structures, the C-terminal hairpin being slightly weaker than the CHC-CTR one (Fig. S4 *b*). Interestingly, the minor S3 population consists of interaction of the 23–30 turn with both termini, which is absent in S1 and S2 structures (Fig. S4 *c*). Representative conformations illustrated in Figs. 2 *a* and S4 support these results.

The S1 and S2 regions in A2V (Figs. 2 *b* and S5, *a* and *b*) and A2T (Figs. 2 *c* and S6, *a* and *b*) monomers show similar features overall when compared to the WT. Interestingly, A2V samples additional structures containing significant Ntr-CHC and CHC-CTR interactions (Fig. 2 *b*, S4 and S5 regions); such conformations are rarely observed for the WT and A2T. The representative structures from those regions imply that a nonpolar amino acid at position 2 (i.e., Val) forms a hydrophobic cluster involving hydrophobic side chains from CHC, resulting in further stabilization of CHC-CTR contacts (Fig. 2 *b*). Accordingly, the secondary-structure analyses and tertiary contact maps for S4 and S5 structures (Fig. 3, *middle* and *right*) reveal

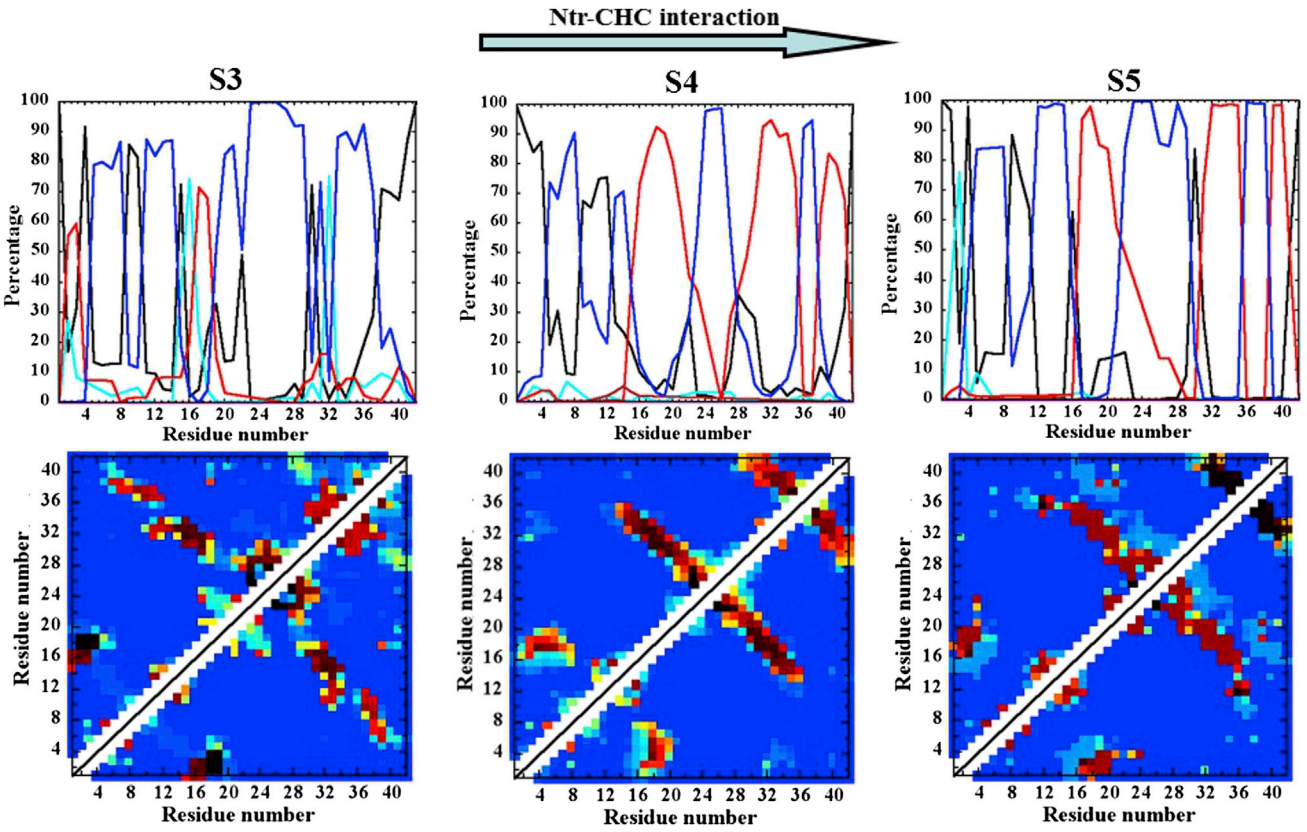

FIGURE 3 Analysis of the A2V conformations with enhanced Ntr-CHC interaction. The residue-based secondary structure and tertiary Cα-Cα contact maps for A2V conformations corresponding to the S3 (*left*), S4 (*middle*), and S5 (*right*) regions. S4 and S5 structures demonstrate double-hairpin topology triggered by Ntr-CHC contacts. Color schemes used are the same as in Figs. 1 and 2. The top arrow indicates the relative probability of Ntr-CHC interaction. To see this figure in color, go online.

double-hairpin-like conformations. Those conformations are regularly populated in A2V (S4 + S5 represent 15% of the total ensemble (Table S1)), as compared with the WT. Lowering of disorder can be seen in those double-hairpin conformations, as revealed from the total number of clusters and the size of the top five clusters (Table S1). Fig. 3 further shows that both sets of hairpin interactions experience a subtle register shift toward the N-terminus in a subpopulation of those double-hairpin structures (the S4 region). The Ntr-CHC contacts are also found in the S3 structures of A2V; however, in those structures, the C-terminus remains in a collapsed coil structure (Fig. 3, *left*).

In sharp contrast, A2T more frequently visits conformations with significant Ntr-CHC interaction but much weaker CHC-CTR contacts (Fig. 2 *c*, *S3 region*). Interestingly, this region of the landscape is rarely populated for both WT and A2V, but the population for A2T is a significant 17% of the total ensemble (Table S1). Further analysis reveals a weaker CHC-CTR interaction resulting in the loss of the first hairpin present in those unique S3 structures (Figs. 2 *c* and 4, *a* and *b*). Consequently, those structures contain only the C-terminal β-hairpin (Fig. 4, *a* and *b*). The side-chain-side-chain contact map illustrates strong interaction between the N-terminus (residues 1–6) and residues 16–22 (Fig. S7); however, residue T2 appears to be weakly involved in those interactions and remains solvent-exposed. In particular, strong D1-K16 and R5-E22 side-chain-side-chain contacts are observed. Accordingly, the representative structure illustrates an ionic network comprised of residues D1, E3, R5, K16, and E22 (Fig. 4 *c*). The salt-bridge population analysis (Table S2) indicates that such ionic interaction becomes more probable in the presence of a solvent-exposed threonine at position 2. For example, the D1-K16 salt bridge is populated with a probability of 34% in S3 structures. At the same time, the formation of the E22-K28 salt bridge becomes less probable (5% (Table S2)) in S3 structures compared to what is observed in S1 and S2 (35% and 12% probabilities, respectively). Taken together, the altered ionic network between the N-terminus and distant charged residues, such as K16 and E22, appears to hinder the formation of the first hairpin interaction in the S3 structures of A2T.

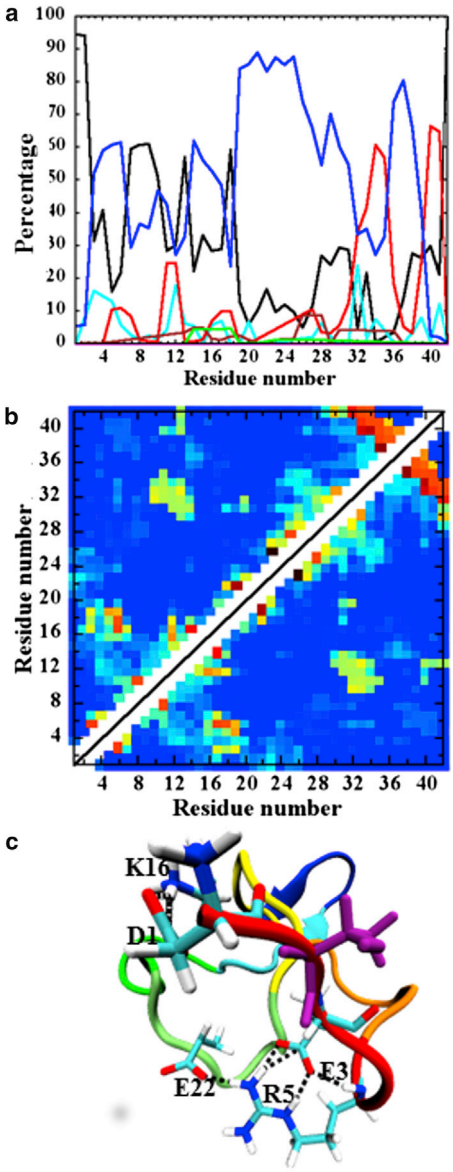

FIGURE 4 Unique A2T conformations with altered ionic network. (*a*) Residue-based secondary structure, (*b*) tertiary Cα-Cα contact map, and (*c*) ionic network within the representative conformation of the largest S3 cluster. The residues, i.e., D1, E3, R5, K16, and E22, forming long-range ionic interaction, are shown using licorice representation. Hydrogen bonds are shown in black dotted lines. Residue Thr2 is shown in purple. Color schemes used are the same as in Figs. 1 and 2. To see this figure in color, go online.

DISCUSSION

Given the reported protective and causative effects associated with A2V and A2T substitutions vis à vis AD, it is of importance to understand the differences in the self-assembly process of those variant peptides, which is intimately associated with the disease pathogenesis. The first step toward this goal is to characterize the conformational landscapes of those variant monomers and compare them with the WT. To our knowledge, this is the first study to compare the structural landscapes of the A2T and A2V $A\beta_{1-42}$ monomers. Our findings from extensive REMD simulations report significant differences in terms of the transient structure population in those variants, which is modulated by interactions of the N-terminus with hydrophobic residues (the CHC) in the case of A2V or with charged residues (K16 and E22) in the case of A2T.

The more persistent β-hairpin character in the hydrophobic regions that lead to a double-hairpin topology in the A2V monomer, as revealed in our simulations, could have important implications in determining the aggregation and

toxicity of A2V. This monomer has been reported to follow a peculiar aggregation behavior that leads to the formation of annular structures with a higher hydrophobicity profile and hence higher toxicity in vitro (39) as well as in vivo (63). A2V also showed greater β-conformation propensity during aggregation (64). The formation of β-structures is believed to be important in amyloid aggregation and toxicity. For example, β-hairpin monomeric conformations in amyloid peptides are found to represent metastable states that interconvert slowly and thus can act as the seed for nucleation (65). Experiments have also highlighted the importance of β-hairpin stabilization in the Aβ monomer in inducing a toxic soluble oligomer population (61,66,67). NMR and atomic force microscopy (AFM) experiments (68) have suggested the presence of double-hairpin conformations within toxic Aβ_{1-42} oligomers. Double-cysteine mutants (Aβ40$_{cc}$ and Aβ42$_{cc}$) with overly stable β-hairpin monomeric conformation have been shown to lower fibril formation and increase populations of toxic β-sheet oligomers and/or protofibrils (67). A structural comparison of monomeric Aβ_{1-42} and fibrillar Aβ_{1-42} suggests that the monomeric hairpin conformation needs to retain sufficient flexibility to undergo a concerted conformational change toward the extended parallel β-sheet structure found in fibrils (61), as also observed in MD simulations of Aβ_{10-35} dimers and trimers (66). The fact that double-hairpin structures were only observed in Aβ_{1-42} and not in Aβ_{1-40} has been linked to the higher aggregation propensity and toxicity of the longer isoform (20). Taken together, our simulations, combined with results of previous studies, imply that the transiently formed double-hairpin structures of the A2V monomer might contribute to the stabilization of small, toxic oligomers composed of β-structures, thus inhibiting fibrillation. Thus, a single-point nonpolar substitution at position 2 of Aβ_{1-42} might act as a switch to redirect the peptides to aggregate via a neurotoxic pathway by stabilizing the β-hairpin conformation (Fig. 5). Our results are consistent with simulations of the shorter A2V Aβ_{1-28} monomer, which indicated that a valine at position 2 can favor Ntr-CHC interaction (69). Nevertheless, the simulations of the full-length A2V peptide presented here demonstrate how the hydrophobic Ntr-CHC interaction can lead to enhanced CHC-CTR hairpin population, leading to the double-hairpin topology (Fig. 5).

Our simulations further suggest a competition between specific hydrophobic and electrostatic interactions modulated by the N-terminus within the Aβ_{1-42} monomer, which in turn regulates the delicate balance among the local minima present in its frustrated conformational landscape (Fig. 5). As discussed above, the N-terminus in the A2V variant stabilizes the double-hairpin conformation by clustering with distant hydrophobic residues (Fig. 5). In contrast, the A2T variant, with its more polar N-terminus, leads to unique structure populations that are rarely seen for the WT and A2V. Although Thr-2 itself minimally interacts with the rest of the protein in those conformations, its presence allows the N-terminus (e.g., residues D1, E3, and R5) to form an unusual set of ionic interactions with distant residues, such as K16 and E22. This effect impairs the formation of the E22-K28 salt-bridge that is known to be crucial for CHC-CTR hairpin formation (18). In consequence, those structures comprise only the C-terminal short β-hairpin (Fig. 5).

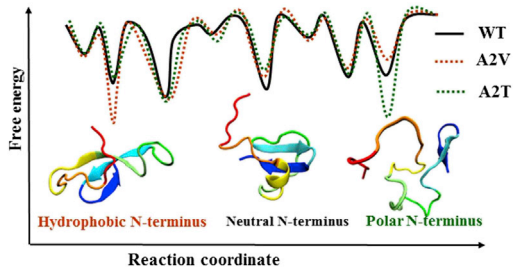

FIGURE 5 Schematic illustration of the Aβ_{1-42} N-terminus influence on the monomeric landscape. The curves show free energy of the variant monomers in one dimension. Based on the analysis, the reaction coordinate might represent a combination of the CHC-CTR interaction and Ntr-peptide interaction. The N-terminal substitution, depending on its hydrophobic or polar nature, can switch the relative population among different β-hairpin conformational states present in the WT landscape. It should be noted that this is an overly simplified representation of the Aβ_{1-42} landscape, and many other conformational states are present due to the intrinsically disordered nature of the system. To see this figure in color, go online.

Mutations at residues E22 (E22K, E22G, and E22Q) and D23 (D23N) that affect Aβ aggregation and cause early-onset AD (15) are reported to alter the WT 21–30 turn structure in simulations (70). Two N-terminal mutations (H6R and D7N) also have been found to affect the extent of β-structure and salt-bridge network within the monomer (71,72). Nevertheless, those mutations directly change the charge distribution within the peptide, which is not the case for A2T. At first glance, a threonine at position 2 would not be expected to have a dramatic effect on the Aβ_{1-42} conformational landscape by altering the electrostatic interaction network. It appears that Thr-2 changes the local conformational preference of the N-terminus, consequently promoting alternative electrostatic interactions that compete with those required for turn nucleation and CHC-CTR hairpin formation. This leads to population of rare and unique conformations (S3 structures). Since β-hairpin abundance has been linked with aggregation mechanisms and toxicity associated with AD (17,73), the unique A2T conformations devoid of the CHC-CTR β-hairpin that also have an altered electrostatic interaction network might contribute toward its slower aggregation (42). It is noteworthy that a threonine in position 2 appears to introduce more disorder within Aβ_{1-42}, whereas a valine at the same position induces some order, which overall is consistent with the intrinsic (dis)order-promoting nature of those amino acids (74). However, our simulations reveal that this effect arises from the global interaction changes triggered by a single

amino acid substitution. Interestingly, conformation-specific antibody staining experiments imply the involvement of the N-terminus in tertiary interactions in the oligomers of both A2V and A2T variants (43). Our simulations demonstrate that such an interaction is also present at the monomer level and is strikingly different between the two variants, which might play a critical role in their early aggregation by populating different monomer structures. Since the Aβ N-terminus also has been suggested to be crucial in binding with membrane (75) and with some toxic Aβ receptors (76), the altered interaction pattern observed in the A2V and A2T monomers may also affect their toxicity (77).

If the interaction between the extreme N-terminus and the rest of the peptide is indeed critical for aggregation and toxicity, then it may be possible, for example, to use small organic molecules (78) and peptides (79,80) that would bind to Aβ monomers and/or oligomers and inhibit aggregation and/or toxicity by intervening in or altering this interaction. The role of the extreme N-terminus in modulating the $A\beta_{1-42}$ monomeric hairpin structure revealed here may guide the design of inhibitory peptides, including variants of the WT (^{1}DAEFRH^{6}) sequence (64).

CONCLUSIONS

Taken together, our findings suggest that the effect of the second amino acid on the $A\beta_{1-42}$ monomer structure is highly complex and sequence-dependent. An enhanced double-hairpin population similar to those reported in toxic WT $A\beta_{1-42}$ oligomers is found in the A2V monomer. Hydrophobic clustering between the N-terminus and the central and C-terminus hydrophobic patches promotes such double-hairpin formation in A2V. In contrast, the A2T mutation triggers unusual ionic interactions of the N-terminus with K16 and E22, thereby impeding CHC-CTR hairpin formation. Consequently, a unique population comprising only the C-terminal hairpin is observed. Although further investigation is needed to obtain a complete molecular picture of the relationship between monomer misfolding, aggregation, and toxicity, and protection against or causation of AD by these N-terminal variants, the simulations described here clearly show that single A2V and A2T substitutions can alter the structural landscape of the $A\beta_{1-42}$ monomer by shifting the equilibrium to different conformational states.

SUPPORTING MATERIAL

Supporting Material, seven figures, and two tables are available at http://www.biophysj.org/biophysj/supplemental/S0006-3495(14)04758-4.

ACKNOWLEDGMENTS

We thank Mirco Sorci for useful discussions and Camilo A. Jimenez Cruz for comments on the manuscript.

Support from IBM BlueGene Science Program is acknowledged.

REFERENCES

1. Selkoe, D. J. 2001. Alzheimer's disease: genes, proteins, and therapy. *Physiol. Rev.* 81:741–766.
2. Klein, A. M., N. W. Kowall, and R. J. Ferrante. 1999. Neurotoxicity and oxidative damage of β amyloid 1–42 versus β amyloid 1–40 in the mouse cerebral cortex. *Ann. N. Y. Acad. Sci.* 893:314–320.
3. Shankar, G. M., B. L. Bloodgood, …, B. L. Sabatini. 2007. Natural oligomers of the Alzheimer amyloid-β protein induce reversible synapse loss by modulating an NMDA-type glutamate receptor-dependent signaling pathway. *J. Neurosci.* 27:2866–2875.
4. Quist, A., I. Doudevski, …, R. Lal. 2005. Amyloid ion channels: a common structural link for protein-misfolding disease. *Proc. Natl. Acad. Sci. USA.* 102:10427–10432.
5. Bonda, D. J., X. Wang, …, M. A. Smith. 2010. Oxidative stress in Alzheimer disease: a possibility for prevention. *Neuropharmacology.* 59:290–294.
6. Sakono, M., and T. Zako. 2010. Amyloid oligomers: formation and toxicity of Aβ oligomers. *FEBS J.* 277:1348–1358.
7. Petkova, A. T., W.-M. Yau, and R. Tycko. 2006. Experimental constraints on quaternary structure in Alzheimer's β-amyloid fibrils. *Biochemistry.* 45:498–512.
8. Sato, T., P. Kienlen-Campard, …, S. O. Smith. 2006. Inhibitors of amyloid toxicity based on β-sheet packing of Aβ40 and Aβ42. *Biochemistry.* 45:5503–5516.
9. Lührs, T., C. Ritter, …, R. Riek. 2005. 3D structure of Alzheimer's amyloid-β_{1-42} fibrils. *Proc. Natl. Acad. Sci. USA.* 102:17342–17347.
10. Petkova, A. T., Y. Ishii, …, R. Tycko. 2002. A structural model for Alzheimer's β -amyloid fibrils based on experimental constraints from solid state NMR. *Proc. Natl. Acad. Sci. USA.* 99:16742–16747.
11. Taylor, B. M., R. W. Sarver, …, D. E. Epps. 2003. Spontaneous aggregation and cytotoxicity of the β-amyloid $A\beta_{1-40}$: a kinetic model. *J. Protein Chem.* 22:31–40.
12. Lazo, N. D., M. A. Grant, …, D. B. Teplow. 2005. On the nucleation of amyloid β-protein monomer folding. *Protein Sci.* 14:1581–1596.
13. Hori, Y., T. Hashimoto, …, T. Iwatsubo. 2007. The Tottori (D7N) and English (H6R) familial Alzheimer disease mutations accelerate Aβ fibril formation without increasing protofibril formation. *J. Biol. Chem.* 282:4916–4923.
14. Bitan, G., M. D. Kirkitadze, …, D. B. Teplow. 2003. Amyloid β -protein (Aβ) assembly: Aβ40 and Aβ42 oligomerize through distinct pathways. *Proc. Natl. Acad. Sci. USA.* 100:330–335.
15. Murakami, K., K. Irie, …, T. Shirasawa. 2003. Neurotoxicity and physicochemical properties of Aβ mutant peptides from cerebral amyloid angiopathy: implication for the pathogenesis of cerebral amyloid angiopathy and Alzheimer's disease. *J. Biol. Chem.* 278:46179–46187.
16. Ono, K., M. M. Condron, and D. B. Teplow. 2010. Effects of the English (H6R) and Tottori (D7N) familial Alzheimer disease mutations on amyloid β-protein assembly and toxicity. *J. Biol. Chem.* 285:23186–23197.
17. Yang, M., and D. B. Teplow. 2008. Amyloid β-protein monomer folding: free-energy surfaces reveal alloform-specific differences. *J. Mol. Biol.* 384:450–464.
18. Baumketner, A., S. L. Bernstein, …, J. E. Shea. 2006. Amyloid β-protein monomer structure: a computational and experimental study. *Protein Sci.* 15:420–428.
19. Urbanc, B., L. Cruz, …, H. E. Stanley. 2004. In silico study of amyloid β-protein folding and oligomerization. *Proc. Natl. Acad. Sci. USA.* 101:17345–17350.
20. Rosenman, D. J., C. R. Connors, …, A. E. García. 2013. Aβ monomers transiently sample oligomer and fibril-like configurations: ensemble characterization using a combined MD/NMR approach. *J. Mol. Biol.* 425:3338–3359.

21. Lam, A. R., D. B. Teplow, …, B. Urbanc. 2008. Effects of the Arctic (E22—>G) mutation on amyloid β-protein folding: discrete molecular dynamics study. *J. Am. Chem. Soc.* 130:17413–17422.

22. Krone, M. G., A. Baumketner, …, J. E. Shea. 2008. Effects of familial Alzheimer's disease mutations on the folding nucleation of the amyloid β-protein. *J. Mol. Biol.* 381:221–228.

23. Ball, K. A., A. H. Phillips, …, T. Head-Gordon. 2011. Homogeneous and heterogeneous tertiary structure ensembles of amyloid-β peptides. *Biochemistry.* 50:7612–7628.

24. Cote, S., P. Derreumaux, and N. Mousseau. 2011. Distinct morphologies for amyloid β protein monomer: $A\beta_{1-40}$, $A\beta_{1-42}$, and $A\beta_{1-40}$ (D23N). *J. Chem. Theory Comput.* 7:2584–2592.

25. Mitternacht, S., I. Staneva, …, A. Irbäck. 2010. Comparing the folding free-energy landscapes of Aβ42 variants with different aggregation properties. *Proteins.* 78:2600–2608.

26. Urbanc, B., L. Cruz, …, N. V. Dokholyan. 2004. Molecular dynamics simulation of amyloid β dimer formation. *Biophys. J.* 87:2310–2321.

27. Takeda, T., and D. K. Klimov. 2009. Probing the effect of amino-terminal truncation for $A\beta_{1-40}$ peptides. *J. Phys. Chem. B.* 113:6692–6702.

28. Scheidt, H. A., I. Morgado, …, D. Huster. 2011. Dynamics of amyloid β fibrils revealed by solid-state NMR. *J. Biol. Chem.* 287:2012–2021.

29. Lv, Z., R. Roychaudhuri, …, Y. L. Lyubchenko. 2013. Mechanism of amyloid β-protein dimerization determined using single-molecule AFM force spectroscopy. *Sci. Rep.* 3:2880.

30. Sarkar, B., V. S. Mithu, …, S. Maiti. 2014. Significant structural differences between transient amyloid-β oligomers and less-toxic fibrils in regions known to harbor familial Alzheimer's mutations. *Angew. Chem. Int. Ed. Engl.* 53:6888–6892.

31. Ma, B., and R. Nussinov. 2011. Polymorphic triple β-sheet structures contribute to amide hydrogen/deuterium (H/D) exchange protection in the Alzheimer amyloid β42 peptide. *J. Biol. Chem.* 286:34244–34253.

32. Zago, W., M. Buttini, …, G. G. Kinney. 2012. Neutralization of soluble, synaptotoxic amyloid β species by antibodies is epitope specific. *J. Neurosci.* 32:2696–2702.

33. Li, H., Z. Du, …, G. Bitan. 2011. C-terminal tetrapeptides inhibit Aβ42-induced neurotoxicity primarily through specific interaction at the N-terminus of Aβ42. *J. Med. Chem.* 54:8451–8460.

34. Maji, S. K., R. R. Ogorzalek Loo, …, D. B. Teplow. 2009. Amino acid position-specific contributions to amyloid β-protein oligomerization. *J. Biol. Chem.* 284:23580–23591.

35. Luheshi, L. M., G. G. Tartaglia, …, D. C. Crowther. 2007. Systematic in vivo analysis of the intrinsic determinants of amyloid β pathogenicity. *PLoS Biol.* 5:e290.

36. Qahwash, I., K. L. Weiland, …, R. Yan. 2003. Identification of a mutant amyloid peptide that predominantly forms neurotoxic protofibrillar aggregates. *J. Biol. Chem.* 278:23187–23195.

37. Jawhar, S., O. Wirths, and T. A. Bayer. 2011. Pyroglutamate amyloid-β (Aβ): a hatchet man in Alzheimer disease. *J. Biol. Chem.* 286:38825–38832.

38. Di Fede, G., M. Catania, …, F. Tagliavini. 2009. A recessive mutation in the APP gene with dominant-negative effect on amyloidogenesis. *Science.* 323:1473–1477.

39. Messa, M., L. Colombo, …, M. Salmona. 2014. The peculiar role of the A2V mutation in amyloid-β (Aβ) 1–42 molecular assembly. *J. Biol. Chem.* 289:24143–24152.

40. Jonsson, T., J. K. Atwal, …, K. Stefansson. 2012. A mutation in APP protects against Alzheimer's disease and age-related cognitive decline. *Nature.* 488:96–99.

41. De Strooper, B., and T. Voet. 2012. Alzheimer's disease: A protective mutation. *Nature.* 488:38–39.

42. Maloney, J. A., T. Bainbridge, …, J. K. Atwal. 2014. Molecular mechanisms of Alzheimer disease protection by the A673T allele of amyloid precursor protein. *J. Biol. Chem.* 289:30990–31000.

43. Benilova, I., R. Gallardo, …, B. De Strooper. 2014. The Alzheimer disease protective mutation A2T modulates kinetic and thermodynamic properties of amyloid-β (Aβ) aggregation. *J. Biol. Chem.* 289:30977–30989.

44. Meinhardt, J., G. G. Tartaglia, …, M. Fändrich. 2007. Similarities in the thermodynamics and kinetics of aggregation of disease-related Aβ (1–40) peptides. *Protein Sci.* 16:1214–1222.

45. Ma, B., and R. Nussinov. 2006. Simulations as analytical tools to understand protein aggregation and predict amyloid conformation. *Curr. Opin. Chem. Biol.* 10:445–452.

46. Kirshenbaum, K., and V. Daggett. 1995. pH-dependent conformations of the amyloid β (1–28) peptide fragment explored using molecular dynamics. *Biochemistry.* 34:7629–7639.

47. Baumketner, A., and J.-E. Shea. 2007. The structure of the Alzheimer amyloid β_{10-35} peptide probed through replica-exchange molecular dynamics simulations in explicit solvent. *J. Mol. Biol.* 366:275–285.

48. Rojas, A. V., A. Liwo, and H. A. Scheraga. 2011. A study of the α-helical intermediate preceding the aggregation of the amino-terminal fragment of the β amyloid peptide ($A\beta_{1-28}$). *J. Phys. Chem. B.* 115:12978–12983.

49. Flöck, D., S. Colacino, …, A. Di Nola. 2006. Misfolding of the amyloid β-protein: a molecular dynamics study. *Proteins.* 62:183–192.

50. Lin, Y.-S., G. R. Bowman, …, V. S. Pande. 2012. Investigating how peptide length and a pathogenic mutation modify the structural ensemble of amyloid β monomer. *Biophys. J.* 102:315–324.

51. Gnanakaran, S., R. Nussinov, and A. E. García. 2006. Atomic-level description of amyloid β-dimer formation. *J. Am. Chem. Soc.* 128:2158–2159.

52. Zhu, X., R. P. Bora, …, R. Prabhakar. 2012. Dimerization of the full-length Alzheimer amyloid β-peptide (Aβ42) in explicit aqueous solution: a molecular dynamics study. *J. Phys. Chem. B.* 116:4405–4416.

53. Fawzi, N. L., K. L. Kohlstedt, …, T. Head-Gordon. 2008. Protofibril assemblies of the arctic, Dutch, and Flemish mutants of the Alzheimer's $A\beta_{1-40}$ peptide. *Biophys. J.* 94:2007–2016.

54. Buchete, N.-V., R. Tycko, and G. Hummer. 2005. Molecular dynamics simulations of Alzheimer's β-amyloid protofilaments. *J. Mol. Biol.* 353:804–821.

55. Convertino, M., R. Pellarin, …, A. Caflisch. 2009. 9,10-Anthraquinone hinders β-aggregation: how does a small molecule interfere with Aβ-peptide amyloid fibrillation? *Protein Sci.* 18:792–800.

56. Chebaro, Y., P. Jiang, …, P. Derreumaux. 2012. Structures of $A\beta_{17-42}$ trimers in isolation and with five small-molecule drugs using a hierarchical computational procedure. *J. Phys. Chem. B.* 116:8412–8422.

57. Das, P., S. G. Kang, …, G. Belfort. 2014. Interaction of amyloid inhibitor proteins with amyloid β peptides: insight from molecular dynamics simulations. *PLoS ONE.* 9:e113041.

58. Jang, H., J. Zheng, and R. Nussinov. 2007. Models of β-amyloid ion channels in the membrane suggest that channel formation in the bilayer is a dynamic process. *Biophys. J.* 93:1938–1949.

59. Jang, H., L. Connelly, …, R. Nussinov. 2013. Mechanisms for the insertion of toxic, fibril-like β-amyloid oligomers into the membrane. *J. Chem. Theory Comput.* 9:822–833.

60. Han, W., and Y. D. Wu. 2005. A strand-loop-strand structure is a possible intermediate in fibril elongation: long time simulations of amyloid-β peptide (10–35). *J. Am. Chem. Soc.* 127:15408–15416.

61. Hoyer, W., C. Grönwall, …, T. Härd. 2008. Stabilization of a β-hairpin in monomeric Alzheimer's amyloid-β peptide inhibits amyloid formation. *Proc. Natl. Acad. Sci. USA.* 105:5099–5104.

62. Yu, L., R. Edalji, …, E. T. Olejniczak. 2009. Structural characterization of a soluble amyloid β-peptide oligomer. *Biochemistry.* 48:1870–1877.

63. Diomede, L., G. Di Fede, …, M. Salmona. 2014. Expression of A2V-mutated Aβ in *Caenorhabditis elegans* results in oligomer formation and toxicity. *Neurobiol. Dis.* 62:521–532.

64. Di Fede, G., M. Catania, …, F. Tagliavini. 2012. Good gene, bad gene: new APP variant may be both. *Prog. Neurobiol.* 99:281–292.

65. Qiao, Q., G. R. Bowman, and X. Huang. 2013. Dynamics of an intrinsically disordered protein reveal metastable conformations that potentially seed aggregation. *J. Am. Chem. Soc.* 135:16092–16101.

66. Larini, L., and J.-E. Shea. 2012. Role of β-hairpin formation in aggregation: the self-assembly of the amyloid-β_{25-35} peptide. *Biophys. J.* 103:576–586.

67. Sandberg, A., L. M. Luheshi, …, T. Härd. 2010. Stabilization of neurotoxic Alzheimer amyloid-β oligomers by protein engineering. *Proc. Natl. Acad. Sci. USA.* 107:15595–15600.

68. Ahmed, M., J. Davis, …, S. O. Smith. 2010. Structural conversion of neurotoxic amyloid-β_{1-42} oligomers to fibrils. *Nat. Struct. Mol. Biol.* 17:561–567.

69. Nguyen, P. H., B. Tarus, and P. Derreumaux. 2014. Familial Alzheimer A2 V mutation reduces the intrinsic disorder and completely changes the free energy landscape of the $A\beta_{1-28}$ monomer. *J. Phys. Chem. B.* 118:501–510.

70. Murray, M. M., M. G. Krone, …, M. T. Bowers. 2009. Amyloid β-protein: experiment and theory on the 21–30 fragment. *J. Phys. Chem. B.* 113:6041–6046.

71. Viet, M. H., P. H. Nguyen, …, M. S. Li. 2014. Effect of the English familial disease mutation (H6R) on the monomers and dimers of Aβ40 and Aβ42. *ACS Chem. Neurosci.* 5:646–657.

72. Viet, M. H., P. H. Nguyen, …, P. Derreumaux. 2013. Effect of the Tottori familial disease mutation (D7N) on the monomers and dimers of Aβ40 and Aβ42. *ACS Chem. Neurosci.* 4:1446–1457.

73. Sgourakis, N. G., Y. Yan, …, A. E. Garcia. 2007. The Alzheimer's peptides Aβ40 and 42 adopt distinct conformations in water: a combined MD/NMR study. *J. Mol. Biol.* 368:1448–1457.

74. Le Gall, T., P. R. Romero, …, A. K. Dunker. 2007. Intrinsic disorder in the protein data bank. *J. Biomol. Struct. Dyn.* 24:325–342.

75. Urbanc, B., M. Betnel, …, G. Bitan. 2011. Structural basis for $A\beta_{1-42}$ toxicity inhibition by Aβ C-terminal fragments: discrete molecular dynamics study. *J. Mol. Biol.* 410:316–328.

76. Kam, T.-I., S. Song, …, Y. K. Jung. 2013. FcγRIIb mediates amyloid-β neurotoxicity and memory impairment in Alzheimer's disease. *J. Clin. Invest.* 123:2791–2802.

77. Hashimoto, Y., and M. Matsuoka. 2014. A mutation protective against Alzheimer's disease renders amyloid β precursor protein incapable of mediating neurotoxicity. *J. Neurochem.* 130:291–300.

78. Bleiholder, C., T. D. Do, …, M. T. Bowers. 2013. Ion mobility spectrometry reveals the mechanism of amyloid formation of $A\beta_{25-35}$ and its modulation by inhibitors at the molecular level: epigallocatechin gallate and scyllo-inositol. *J. Am. Chem. Soc.* 135:16926–16937.

79. Gessel, M. M., C. Wu, …, M. T. Bowers. 2012. $A\beta_{39-42}$ modulates Aβ oligomerization but not fibril formation. *Biochemistry.* 51:108–117.

80. Esteras-Chopo, A., G. Morra, …, G. Colombo. 2008. A molecular dynamics study of the interaction of D-peptide amyloid inhibitors with their target sequence reveals a potential inhibitory pharmacophore conformation. *J. Mol. Biol.* 383:266–280.

Supplementary Information

Alzheimer's Protective A2T mutation changes the conformational landscape of the $A\beta_{1\text{-}42}$ monomer differently than does the A2V mutation

Payel Das[1*], Brian Murray[2], Georges Belfort[2]

[4]Soft Matter Theory and Simulations Group, Computational Biology Center, IBM Thomas J. Watson Research Center, Yorktown Heights, NY 10598.

[2]Howard P. Isermann Department of Chemical and Biological Engineering, and Center for Biotechnology and Interdisciplinary Studies, Rensselaer Polytechnic Institute, Troy, New York 12180-3590.

Model and methods

The monomeric conformational ensembles were generated by performing replica-exchange molecular dynamics (REMD) simulations of the solvated peptides using the GROMACS4 software [1]. REMD is an enhanced sampling algorithm that helps the system to escape the local minima in the free energy landscape by increasing temperature [2]. The method consists of several identical copies or replicas of the system, which are simulated in parallel over a range of temperatures. At frequent intervals, trials to exchange the temperature of all neighboring replicas are performed, according to a Metropolis Monte Carlo criterion. The swapping probability is chosen to satisfy a detailed balance. This method has been successfully applied to construct the ensemble of intrinsically disordered peptides that lack a single native conformation and instead populate multiple rapidly interchanging states, such as Aβ at atomic resolution [3-6].

The following protocol was used to construct the initial conformation for REMD simulations for each variant peptide: first, a 10 ns MD simulation at high temperature (~700 K) in vacuum was performed starting from a fully extended peptide conformation with charged termini. The collapsed peptide was solvated in a 56 x 56 x 56 $Å^3$ cubic box containing ~5,600 water molecules. The protonation states of the acidic and basic residues of the peptide were set at pH 7 and three Na^+ ions were added to neutralize the charge. The solvated peptide was equilibrated for 2 ns in an NPT ensemble (300 K and 1 atm) before the REMD run. Finally, constant volume REMD simulations were run for 175 ns per replica with an integration step of 2 ns, resulting in an aggregate simulation time of 11.2 μs per system. A total of 64 replicas within an exponentially distributed temperature range [7] of 276-592 K were used for each system and the replica exchange attempts were made every 4 ps. Use of this protocol results in the average exchange ratio of 19% that is constant over the temperature range. The system was coupled to a Nose-Hoover heat bath to maintain constant temperature between swaps. The particle-mesh Ewald (PME) method was used for the long-range electrostatic interactions [8], while the van der Waals interactions were treated with a cut-off distance of 10 Å. The bonds were constrained using LINCS [9] and SETTLE [10] algorithms. For all calculations, a combination of OPLS-AA force-field [11] and TIP3P water model [12] was used. This combination has been reported to generate the structural ensemble that is in agreement with NMR experiments [13].

All MD simulations were run using IBM BlueGene/Q supercomputers. The convergence of the simulations was checked by dividing the simulation data in two or four equal sets and estimating the similarity of the secondary/tertiary structure obtained from those sets. The secondary structure was estimated using the STRIDE program [14]. A cutoff distance of 8 Å between C_α atoms was considered to define a contact between two residues. Only non-sequential contacts ($|i-j| \geq 3$) were considered for tertiary interactions. For contacts between side-chains of two residues, a cutoff distance of 5 Å (heavy atom only) was used. Hydrogen bonds were determined with a cutoff of 3.5 Å for the donor-acceptor distance and a cutoff of 30° for the donor-hydrogen-acceptor angle.

Potential of mean force (PMF, W(X)) plots were obtained from a histogram analysis, using the equation $W(X) = -RT \log(p(X))$, where X is the set of reaction coordinates and p(X) is the probability. The number of contacts between the N-terminus (residues 1-5) and CHC (residues 16-21), termed as $NC_{Ntr\text{-}CHC}$, and the number of contacts between the CHC and C-terminus (residues 31-42), termed as $NC_{CHC\text{-}CTR}$, were used as the reaction coordinates for PMF estimation. A cluster analysis using the Daura algorithm [15] was performed. A 3 Å C_α-RMSD cut-off between two conformations was used for cluster analysis of the highly populated regions on the PMF plots. Regions on the PMF plots that individually represent ≥5% of total production ensemble were only considered for further analysis. The criteria used to define those regions can be found in Table S1. All peptide structure figures were rendered using VMD [16].

Equilibration and validation of the REMD ensemble

To make sure that the choice of the initial structure did not affect our results, C_α root-mean-square-distance (RMSD) from the initial structure was estimated as a function of the simulation time for the 305 K replica for all three variants (**Fig. S1a**). The RMSD reaches a sufficiently high value of 20 Å with first 15 ns of simulation and then fluctuates around that value for each variant, suggesting that the structural ensemble populated after 15 ns is independent of the initial structure.

Figure S**1b-c** shows the evolutions of radius of gyration, Rg, and turn propensities of the 305 K trajectory for each variant. Rg reaches an average value of ~10-11 Å after ~60 ns, at what point the turn propensity steadily fluctuates around ~50%, for all three variants. Thus, the first 60 ns of each replica was discarded as the equilibration time and the 60-175 ns portion of the twelve REMD simulation trajectories in 276-308 K temperature range was considered as the production ensemble comprised of ~28,000 conformations. We validate the simulated WT ensemble by comparing the $^3J_{HNHA}$ couplings derived from backbone ϕ dihedrals in simulations with NMR experiments [17]. **Figure S1d** shows the comparison between the simulated $^3J_{HNHA}$ couplings back-calculated from the production period of the 278 K replica of WT and experiments using the three different parameter sets for the Karplus equation [17]. The set proposed in Vuister and Bax [18] produces universally high MD-derived J-coupling values, implying that simulations might have over-sampled β-conformations, and yields an RMSD of 1.16 Hz. On the other hand, use of parameters for WT $A\beta_{1-42}$ proposed in Sgourakis et al. [19] and Rosenman et al. [17] produces lower RMSD values (0.91 Hz and 0.94 Hz, respectively) and better agreement with the experimental values. This is because of the fact that the Vuister and Bax's parameters were determined by fitting to well-ordered X-ray structures, whereas the parameters proposed in Sgourakis et al. [19] and Rosenman et al. [17] account for the motional averaging effect within a MD dataset. The residues that show strongest deviation (>1 Hz) from the corresponding experimental value are F4, H13, A21, and S26. It is interesting that the J-coupling values obtained for S26 from two different NMR pulse sequences – HNHA [19] and J-resolved SOFAST-HMQC [17] (shown in Fig. 1c, black line) - also vary significantly. The discrepancy between experimental and MD-derived J-couplings for F4, H13, and A21 could be due to the force-field limitation.

Additional ensemble properties

The Rg distributions show a single peak at ~10-11 Å for all three variants (**Fig. S2a**), indicating a collapsed coil structure (the value for the statistical coil is ~20 Å). This value is also consistent with what has been reported before for the WT monomer in simulations and experiments [20, 21]. A cluster analysis on the production ensemble (**Fig. S2b**) reveals that the top 50 clusters only represent ~20% of the population for all three systems, suggesting their intrinsic disordered nature. The fact that a lower C_α-RMSD cutoff (4.5 Å) for the A2V system can be used to produce similar results compared to the WT and A2T peptides (6 Å cutoff) suggests relative lowering of disorder in A2V.

Convergence of the secondary and tertiary structure estimated from REMD

To determine whether the sampling has converged or not in terms of the secondary structure propensity, the 60-175 ns production ensemble was divided in four equal ~25 ns long segments and the standard deviation values were estimated (**Fig. S3a**). Overall, the values of standard deviations appear small. It was earlier reported that the β-content is the slowest to converge [17]. **Fig. S3a** confirms that the standard error for the β-element composition is small enough (1.6%, 1.4%, and 1.9% for WT, A2V, and A2T, respectively). The sampling convergence in terms of the tertiary structure was checked by dividing

the simulation data in two ~55 ns equal segments and comparing the tertiary structure obtained from those sets. The results are shown in **Fig. S3c-e**. No new major features were obtained by doing so, suggesting reasonable convergence of the tertiary structure. To confirm that 175 ns per replica produces a good representation of the structural ensemble of the monomeric variants, we extended the simulations for each system for another 50 ns, resulting 225 ns per replica and compared with results obtained from 60-175ns portion. The secondary and tertiary structure distributions from the extended runs are shown in Figures **S3b** and **S3c-e** (bottom). Overall, the composition and major features remain unchanged and only subtle changes are detected, suggesting that the structural ensemble generated by the procedure described in the manuscript has reached a steady state in terms of secondary and tertiary structures and provides a good representation of the peptide variant monomers in solution.

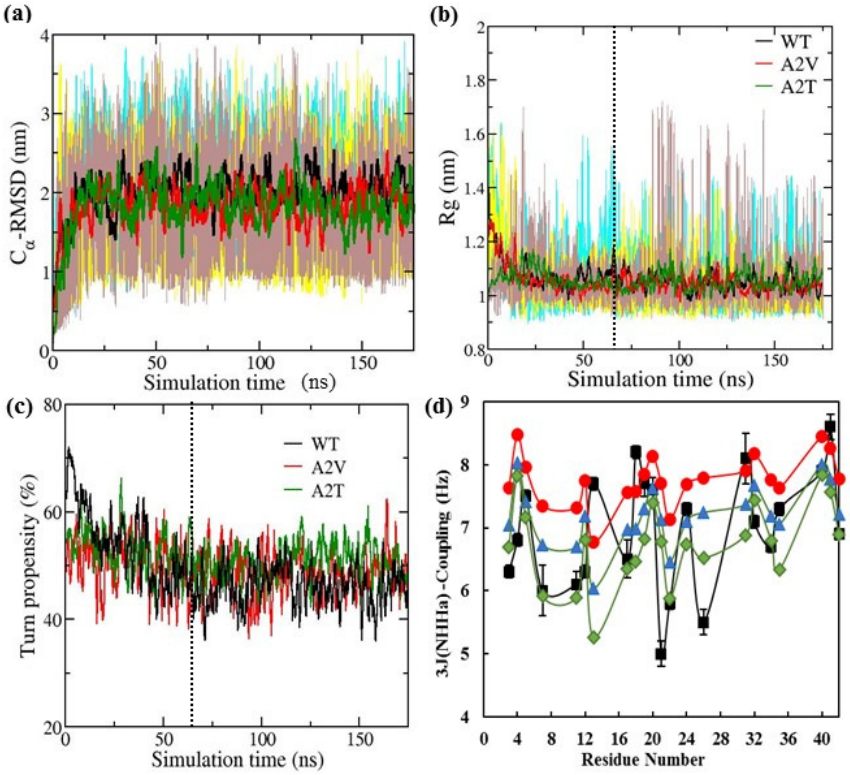

Figure S1: Equilibration and validation of REMD trajectories. (a) Evolution of the C_α root-mean-square-distance (RMSD) from the initial structure for the trajectories at 305 K (black: WT; red: A2V; green: A2T). Moving averages of 1 ns are shown. The raw data (cyan: WT; yellow: A2V; brown: A2T) are also shown. **(b-c)** Evolutions of the radius of gyration, Rg, and turn propensity, for the trajectories at 305 K (black: WT; red: A2V; green: A2T). Moving averages of 1 ns are shown. The raw data (cyan: WT; yellow: A2V; brown: A2T) are also shown in (b). The black dotted lines indicate equilibration around 60 ns. **(d)** Comparison between experimental $^3J_{HNHA}$ couplings (black) and MD-derived corresponding values (red: Vuister parameters; green: Sgourakis parameters; blue: Rosenman parameters) back-calculated from the production period of the WT 278K replica.

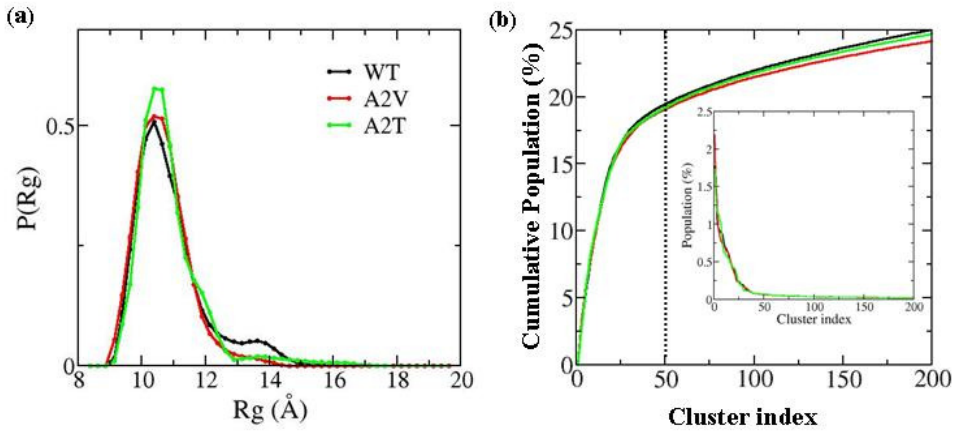

Figure S1. (a). Rg distributions and (b) Cluster analysis. **(a)** Normalized Rg histograms for three variant monomers (black: WT; red: A2V; green: A2T), as obtained from REMD. **(b)** Cumulative population (in %) of the top 200 clusters for each system (black: WT; red: A2V; green: A2T), as obtained using the greedy algorithm with a Cα–RMSD cutoff of 6 Å for the WT and A2T systems and of 4.5 Å for the A2V systems. The black dotted line indicates that top 50 clusters represent only ~20% of the total population for all three systems. **Inset.** Individual population (in %) of the top 200 clusters as a function of cluster index.

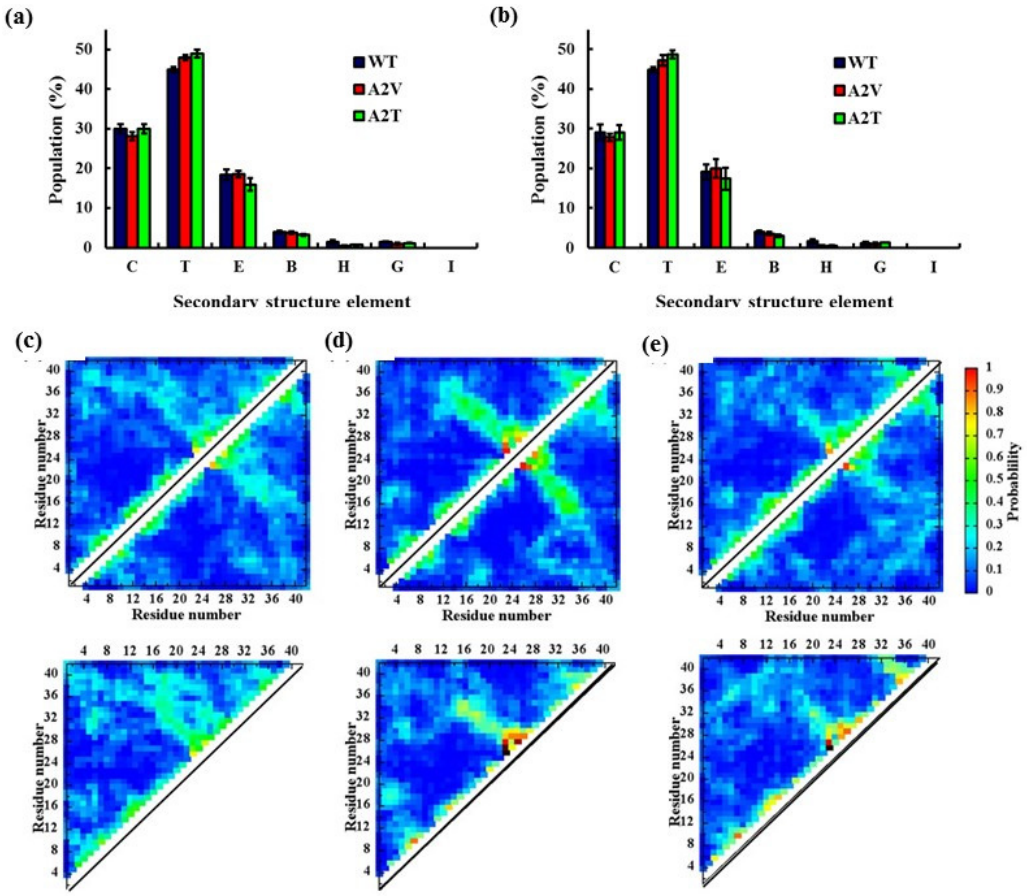

Figure S3: Convergence of the secondary and tertiary structure. The ensemble-averaged percentage population of each secondary structural element averaged over all residues. Results obtained from the production ensemble (60-175 ns of 276-308 K replicas) are shown in **(a)**, whereas results obtained from the extended runs (60-225 ns of 276-308 K replicas) are shown in **(b)**. The standard deviations were estimated by splitting the data in four (b) or six (c) equal ~25 ns long segments. Results on the convergence of tertiary contact distribution is shown in **(c-e)**, WT **(c)**, A2V **(d)**, A2T **(e)**. Top panel: The data from the production ensemble (60-175 ns of 276-308 K replicas) were divided into two equal ~55 ns long subsets (shown in upper and lower triangles of the contact maps) and the probabilities were averaged over each of the subsets. Bottom panel: Results obtained from the extended runs (175-225 ns portion of 276-308 K replicas). Color scheme used is same as in Fig.1d-f. No new major features were obtained by doing so, suggesting reasonable sampling convergence of the REMD simulations.

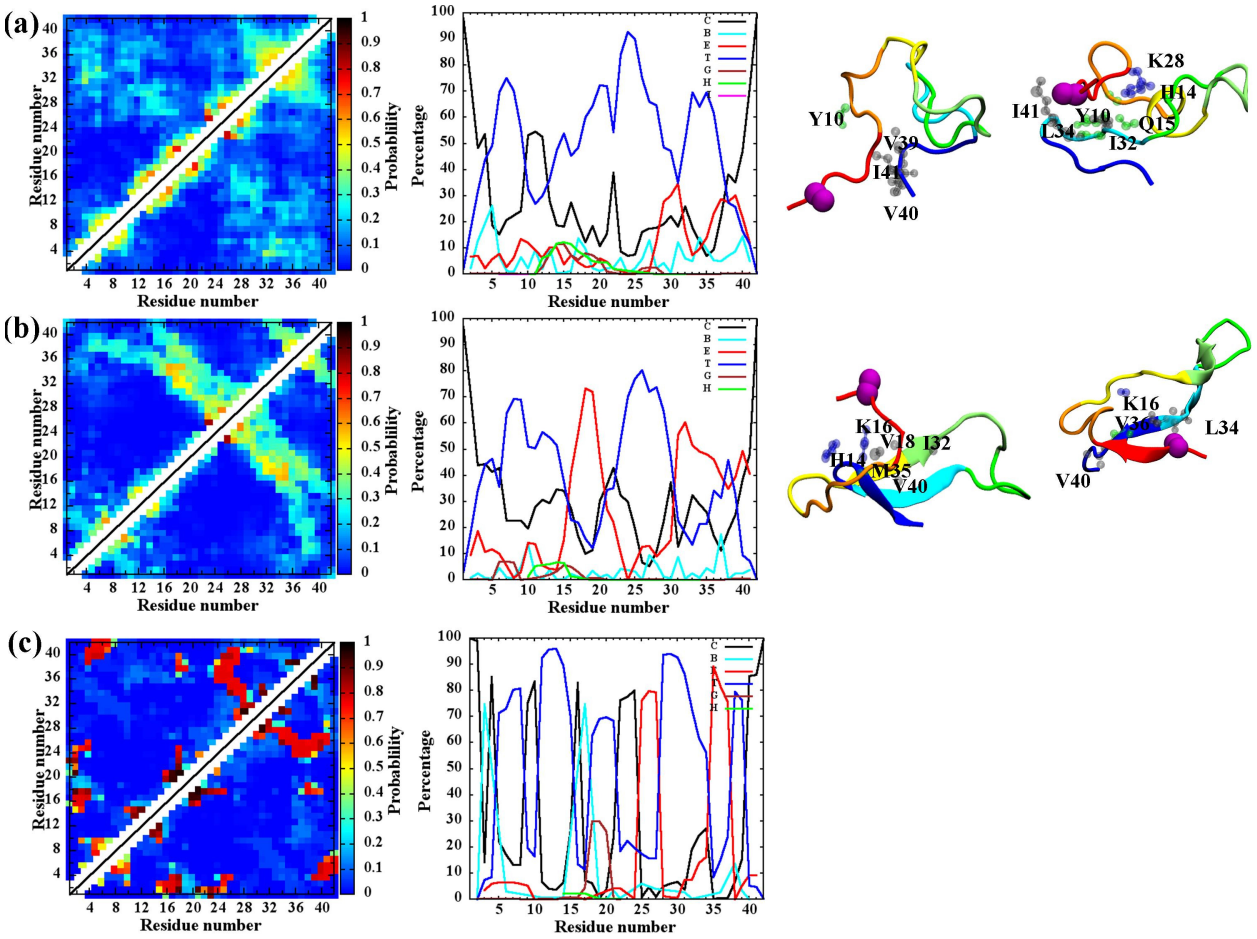

Figure S4: **Structural analyses of the most populated regions of the WT PMF plot (Fig. 2a).** The tertiary contact maps and the residue-based secondary structure for conformations corresponding to the **(a)** S1 region, **(b)** S2 region, and **(c)** S3 region for the WT peptide. S1 region represents structures with limited CHC-CTR and Ntr-CHC contacts. The structures with robust CHC-CTR interaction and a few (≤5) Ntr-CHC contacts are represented by the S2 region. Conformations with stronger Ntr-CHC interaction that lacked substantial CHC-CTR contacts are represented by the weakly populated S3 region. The representative conformations of the second and third largest clusters are also shown for the S1 and S2 regions along with residues forming contacts with the Ntr region. Color schemes used for the figures are the same as in Fig. 1-2.

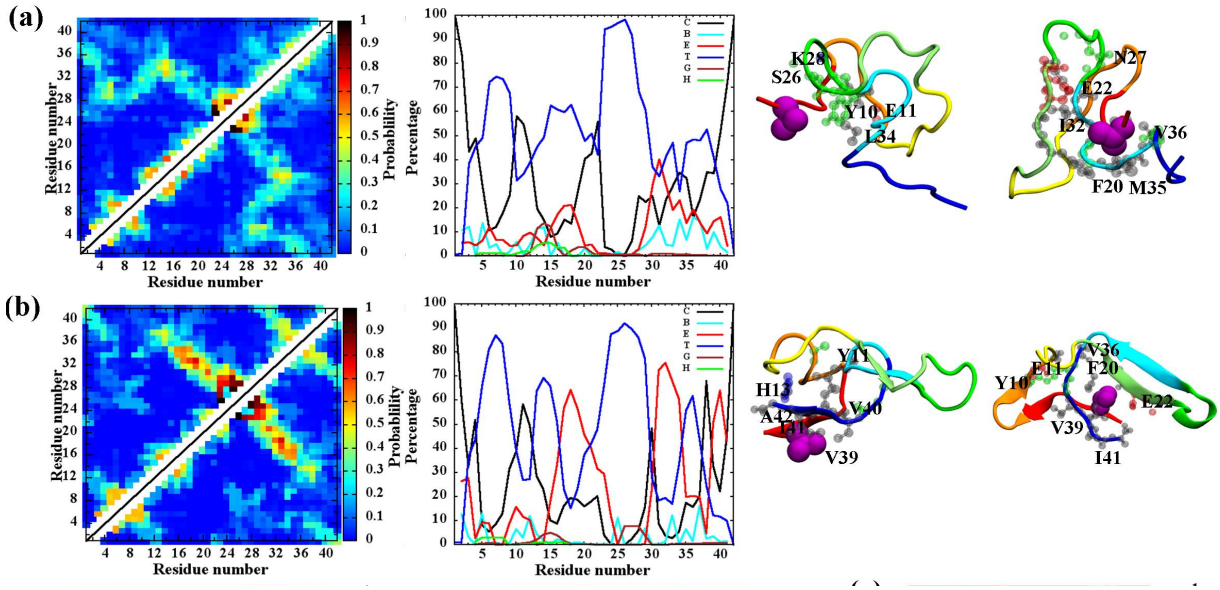

Figure S5: **Structural analyses of the S1 and S2 regions of the A2V PMF plot (Fig. 2b).** The tertiary contact maps and the residue-based secondary structure for conformations corresponding to the **(a)** S1 region, and **(b)** S2 region for the A2V peptide. The representative conformations of the second and third largest cluster are also shown for the S1 and S2 regions along with residues forming contacts with the Ntr region. Color schemes used for the figures are the same as in Fig 1-2.

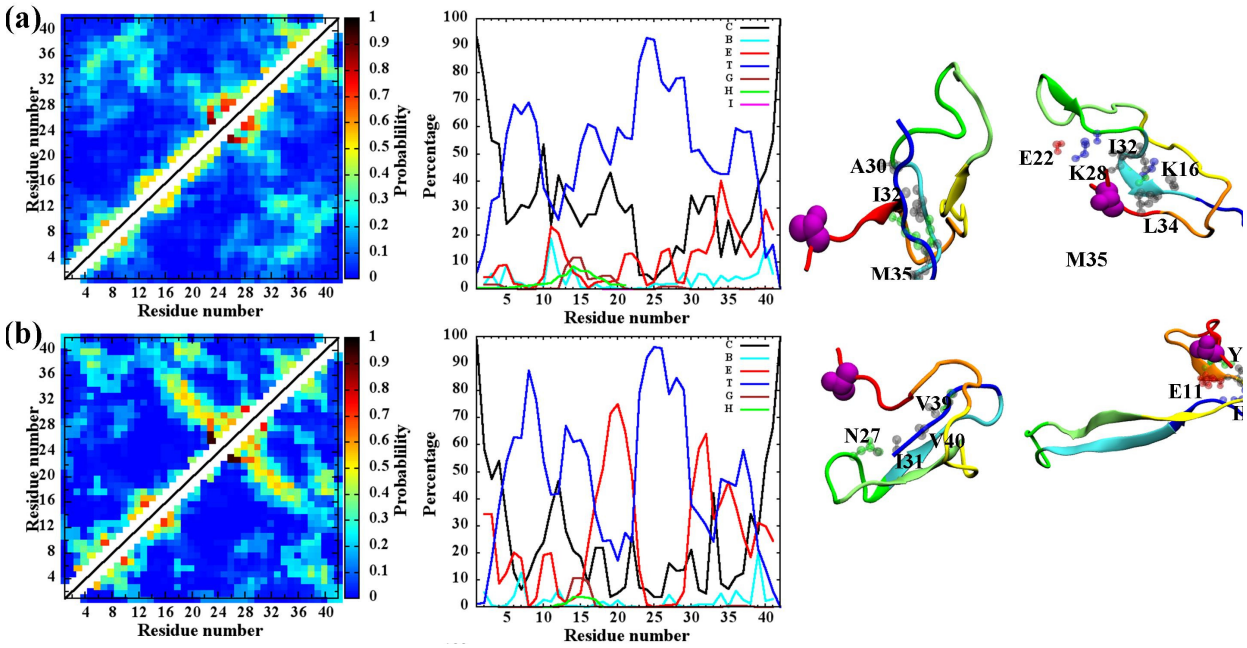

Figure S6: **Structural analyses of the S1 and S2 regions of the A2T PMF plot (Fig. 2c).** The tertiary contact maps and the residue-based secondary structure for conformations corresponding to the **(a)** S1 region, and **(b)** S2 region for the A2T peptide. The representative conformations of the second and third largest cluster are also shown for the S1 and S2 regions along with residues forming contacts with the Ntr region. Color schemes for the figures are the same as in Fig 1-2.

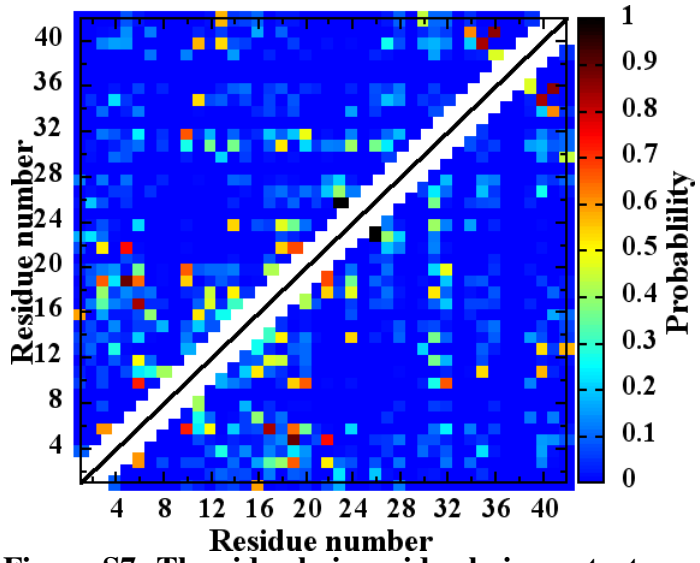

Figure S7: The side-chain—side-chain contact map for the S3 population of A2T. A cutoff of 5 Å was used for defining a contact between side-chains of two residues.

Table S1: Definition of summary of cluster analysis results for S1-S5 regions of all three variants (Fig. 2). NC1 and NC2 represent number of contacts between Ntr-CHC and CHC-CTR, respectively. Regions on the PMF plots that individually represent ≥5% of total production ensemble are only considered. The numbers within parentheses represent the population using the following criteria: S1 (NC1=[0-2], NC2=[0-13]); S2 (NC1=[0-2], NC2=[14-25]); S3=(NC1=[2-15], NC2=[0-10]).

WT	S1 NC1 = [0-2] NC2 = [0-13]	S2 NC1 = [0-2] NC2 = [14-25]	S3 NC1 = [8-11] NC2 = [0-9]	S4	S5
% of total population	32.6	35.9	6.6 (11.4)	N/A	N/A
# clusters	105	107	8		
Size of top five clusters (%)	7.6 6.5 6.0 5.4 5.2	14.3 11.1 7.7 6.9 6.3	76.4 8.0 5.8 4.5 3.3		
A2V	S1 NC1 = [0-3] NC2 = [0-13]	S2 NC1 = [0-1] NC2 = [14-25]	S3 NC1 = [11-15] NC2 = [4-11]	S4 NC1 = [5-13] NC2 = [13-17]	S5 NC1 = [10-13] NC2 = [19-25]
% of total population	40.1 (38.6)	24.9 (25.6)	5.9 (9.1)	9.1	5.5
# clusters	127	78	7	23	6
Size of top five clusters (%)	10.7 8.9 8.6 6.7 5.7	15.6 13.3 13.1 11.6 10.3	79.0 8.6 6.2 4.2 1.6	57.8 11.6 5.5 3.6 3.6	83.7 14.9 0.8 0.3 0.1
A2T	S1 NC1 = [0-2] NC2 = [0-13]	S2 NC1 = [0-3] NC2 = [14-25]	S3 NC1 = [2-10] NC2 = [0-5]	S4 NC1 = [5-7] NC2 = [17-20]	S5 NC1 = [2-4] NC2 = [24-26]
% of total population	40.1 (40.1)	25.6 (24.9)	17.2 (21.5)	N/A	N/A
# clusters	137	68	36		
Size of top five clusters (%)	11.4 9.7 8.3 7.2 4.3	20.9 18.2 10.5 8.7 4.2	41.2 9.2 7.7 6.8 6.5		

Table S2: Probability (in %) of non-sequential salt-bridges between all charged residues for S1-S5 regions for all three variants. Those with probability <1% re marked as "-". The salt-bridges involving D1 and R5 (N-terminal residues) that are frequently formed in the S3 structures of the WT or the A2T monomer (**Fig. 2a & Fig. 2c**) are marked red.

	WT	S1	S2	S3	S4	S5
WT	D1-R5	12.8	2.7	-	N/A	N/A
	D1-K16	2.4	20.6	67.4		
	D1-K28	5.8	2.9	7.8		
	E3-K16	3.0	4.2	-		
	E3-K28	1.7	-	2.0		
	R5-E11	-	4.7	-		
	R5-E22	4.0	2.4	-		
	R5-D23	4.0	-	-		
	D7-K16	6.2	8.2	1.9		
	D7-K28	4.1	-	-		
	E11-K16	4.9	-	3.0		
	E11-K28	4.7	-	-		
	K16-E22	8.3	1.7	5.4		
	K16-D23	6.0	-	-		
	E22-K28	16.7	14.3	3.2		
	D23-K28	3.2	9.7	-		
A2V	D1-R5	-	-	-	9.7	-
	D1-K16	7.6	1.4	2.7	8.6	13.1
	D1-K28	3.8	6.3	-	-	-
	E3-K16	-	-	3.3	-	-
	E3-K28	-	-	-	-	-
	R5-E11	3.2	4.9	3.7	-	-
	R5-E22	1.8	-	-	-	-
	R5-D23	-	-	-	-	-
	D7-K16	2.5	-	2.9	40.5	-
	D7-K28	5.7	-	-	-	-
	E11-K16	15.0	21.9	4.1	5.8	-
	E11-K28	9.9	-	-	-	-
	K16-E22	11.6	-	-	-	-
	K16-D23	-	-	-	-	-
	E22-K28	29.3	25.8	16.4	12.6	9.6
	D23-K28	-	-	-	-	-
A2T	D1-R5	4.5	-	-	N/A	N/A
	D1-K16	4.2	8.5	33.8		
	D1-K28	6.2	2.0	5.7		
	E3-K16	-	-	-		
	E3-K28	4.0	-	-		
	R5-E11	1.2	-	-		
	R5-E22	1.5	1.8	7.8		
	R5-D23	1.0	6.3	-		
	D7-K16	-	-	3.3		
	D7-K28	-	6.3	-		
	E11-K16	18.6	3.2	15.3		
	E11-K28	9.1	5.4	-		
	K16-E22	7.2	1.2	-		
	K16-D23	-	-	-		
	E22-K28	35.5	12.4	5.6		
	D23-K28	1.5	2.0	1.6		

References

1. Hess, B., et al., *GROMACS 4: Algorithms for highly efficient, load-balanced, and scalable molecular simulation*. Journal of Chemical Theory and Computation, 2008. **4**(3): p. 435-447.
2. Sugita, Y. and Y. Okamoto, *Replica-exchange molecular dynamics method for protein folding*. Chemical Physics Letters, 1999. **314**(1-2): p. 141-151.
3. Fukunishi, H., O. Watanabe, and S. Takada, *On the Hamiltonian replica exchange method for efficient sampling of biomolecular systems: Application to protein structure prediction*. Journal of Chemical Physics, 2002. **116**(20): p. 9058-9067.
4. Miyashita, N., J.E. Straub, and D. Thirumalai, *Structures of beta-amyloid peptide 1-40, 1-42, and 1-55-the 672-726 fragment of APP-in a membrane environment with implications for interactions with gamma-secretase*. J Am Chem Soc, 2009. **131**(49): p. 17843-52.
5. Qiao, Q., G.R. Bowman, and X. Huang, *Dynamics of an intrinsically disordered protein reveal metastable conformations that potentially seed aggregation*. J Am Chem Soc, 2013. **135**(43): p. 16092-101.
6. Sgourakis, N.G., et al., *Atomic-level characterization of the ensemble of the Abeta(1-42) monomer in water using unbiased molecular dynamics simulations and spectral algorithms*. J Mol Biol, 2011. **405**(2): p. 570-83.
7. Patriksson, A. and D. van der Spoel, *A temperature predictor for parallel tempering simulations*. Physical Chemistry Chemical Physics, 2008. **10**(15): p. 2073-2077.
8. Deserno, M., Holm, C. , *How to mesh up Ewald sums. II. An accurate error estimate for the particleâ€“particleâ€“particle-mesh algorithm*. The Journal of Chem.. Phys., 1998. **109**: p. 8.
9. Hess, B., et al., *LINCS: A linear constraint solver for molecular simulations*. Journal of Computational Chemistry, 1997. **18**(12): p. 1463-1472.
10. Miyamoto, S. and P.A. Kollman, *Settle: An analytical version of the SHAKE and RATTLE algorithm for rigid water models*. Journal of Computational Chemistry, 1992. **13**(8): p. 952-962.
11. Jorgensen, W.L., D. Maxwell, and J. Tirado-Rives, *Development and testing of the OPLS all-atom force field on confromational energetics and properties of organic liquids*. J. Am. Chem. Soc., 1996. **118**: p. 11225-11236.
12. Jorgensen, W.L., et al., *Comparison of simple potential functions for simulating liquid water*. J Chem Phys, 1983. **79**: p. 926-935.
13. Rosenman, D.J., et al., *Abeta Monomers Transiently Sample Oligomer and Fibril-Like Configurations: Ensemble Characterization Using a Combined MD/NMR Approach*. Journal of Molecular Biology, 2013. **425**(18): p. 3338-3359.
14. Frishman, D. and P. Argos, *Knowledge-based protein secondary structure assignment*. Proteins, 1995. **23**(4): p. 566-579.
15. Daura, X., et al., *Peptide Folding: When Simulation Meets Experiment*. Angewandte Chemie International Edition, 1999. **38**(1-2): p. 236-240.
16. Humphrey, W., A. Dalke, and K. Schulten, *VMD: visual molecular dynamics*. Journal of molecular graphics, 1996. **14**(1): p. 33-38.

17. Rosenman, D.J., et al., *Abeta Monomers Transiently Sample Oligomer and Fibril-Like Configurations: Ensemble Characterization Using a Combined MD/NMR Approach*. J Mol Biol, 2013. **425**(18): p. 3338-3359.
18. Vuister, G.W. and A. Bax, *Quantitative J Correlation - a New Approach for Measuring Homonuclear 3-Bond J(H(N)H(Alpha) Coupling-Constants in N-15-Enriched Proteins*. Journal of the American Chemical Society, 1993. **115**(17): p. 7772-7777.
19. Sgourakis, N.G., et al., *Atomic-level characterization of the ensemble of the Abeta (1-42) monomer in water using unbiased molecular dynamics simulations and spectral algorithms*. Journal of molecular biology, 2011. **405**(2): p. 570-583.
20. Nag, S., et al., *Nature of the Amyloid-beta Monomer and the Monomer-Oligomer Equilibrium*. Journal of Biological Chemistry, 2011. **286**(16): p. 13827-13833.
21. Baumketner, A., et al., *Amyloid β-protein monomer structure: A computational and experimental study*. Protein Science, 2006. **15**(3): p. 420-428.